OPEN ACCESS
IOP Publishing
Plasma Physics and Controlled Fusion
Plasma Phys. Control. Fusion **66** (2024) 125001 (9pp)
https://doi.org/10.1088/1361-6587/ad85f8

Utilizing parametric instabilities to diagnose edge density fluctuations in TCV

A Clod[1,*], R Ragona[1], M G Senstius[2], T Jensen[1], U Kumar[3], S Coda[3], S K Nielsen[1] and the TCV Team[4]

[1] Department of Physics, Technical University of Denmark, Fysikvej, DK-2800 Kongens Lyngby, Denmark
[2] Rudolf Peierls Centre for Theoretical Physics, University of Oxford, Oxford OX1 3NP, United Kingdom
[3] École Polytechnique Fédérale de Lausanne (EPFL), Swiss Plasma Center (SPC), CH-1015 Lausanne, Switzerland

E-mail: aclpe@dtu.dk

Received 10 July 2024, revised 20 September 2024
Accepted for publication 11 October 2024
Published 22 October 2024

Abstract
Two-plasmon decay instabilities (TPDIs) are a class of parametric instabilities where a gyrotron beam, polarized in X-mode, decays nonlinearly into two upper hybrid waves at approximately half frequency. Here, we present the design of a simple radiometer that was installed at Tokamak á configuration variable to diagnose TPDIs as well as a novel technique that was used to calibrate the radiometer using thermal electron cyclotron emissions. We show examples of measured radiation from TPDIs that occur when the gyrotron beam intersects blob filaments in the scrape-off layer and demonstrate that the frequency separation of the TPDI daughter waves can be used to assess the densities of the blob filaments. This technique could be utilized to diagnose density fluctuations due to both blobs, ELMs, and rotating magnetic islands.

Keywords: three-wave interaction, two-plasmon decay, parametric decay instability, electron cyclotron resonance heating, electron Bernstein wave, upper hybrid wave, blob diagnostic

1. Introduction

One of the main external heating systems in magnetic confinement fusion devices such as tokamaks and stellarators is electron cyclotron resonance heating (ECRH), where high-intensity microwave beams from gyrotrons couple resonantly to the cyclotron motion of electrons in the plasma. In most plasma temperature and density regimes, the propagation of gyrotron beams is linear. Under certain conditions, however, a gyrotron beam can undergo a nonlinear parametric decay instability (PDI) [1], where energy is transferred from the main beam to two other linear plasma waves.

One class of PDIs is called the two-plasmon decay instability (TPDI). The term was originally reserved for describing the parametric decay of an incident light wave into two half-frequency Langmuir waves in unmagnetized inertial confinement fusion experiments [2]. It has since been extended to also cover the parametric decay of an incident gyrotron beam, polarized in X-mode, into two approximately half-frequency upper hybrid (UH) waves [3, 4] during ECRH.

The first experimental indications of TPDIs during ECRH were measurements of anomalous back-scattering when an X2 beam crossed a rotating magnetic island in TEXTOR [5, 6]. This anomalous back-scattering with frequencies around the

[4] See Reimerdes *et al* 2022 (https://doi.org/10.1088/1741-4326/ac369b) for the TCV Team.
[*] Author to whom any correspondence should be addressed.

gyrotron frequency is thought to be generated in secondary recombination processes after TPDIs, in accordance with recent modelling [7]. Similar radiation attributed to TPDIs were later observed at Wendelstein 7-X [8, 9] and ASDEX Upgrade [10], where half-frequency emissions were also observed. All mentioned measurements were obtained using complicated collective Thomson scattering (CTS) systems [11].

The Tokamak á configuration variable (TCV) [12] is a medium-sized versatile device with a large ECRH power density, making it ideal for studying TPDIs. A new dedicated radiometer was developed to measure direct radiation from primary TPDI daughter waves around half gyrotron frequency. This diagnostic produced the first detailed measurements of separate daughter waves from TPDIs in the scrape-off layer (SOL) of a tokamak, correlated with both blobs and ELM activity [13].

In this paper, we provide details on the design of the radiometer, which was connected to an already existing transmission line. The radiometer was calibrated using measurements of thermal electron cyclotron emissions (ECE) combined with estimates of the radiation temperature from a ray tracing analysis with a method specified in this paper.

In addition to detailing the configuration of the radiometer, we provide examples of measurements of separate TPDI daughter waves and demonstrate that radiation from TPDIs is detected when blob filaments pass the gyrotron beam. We further demonstrate that the frequency separation of the TPDI daughter waves contains information on the density of the passing blobs. By analysing the frequency separation as well as signal lengths, we propose that measurements of radiation from TPDIs can be utilized as a non-invasive diagnostic for assessing density fluctuations due to e.g. blobs and ELMs.

2. TPDI

The TPDI, relevant for ECRH, is a parametric three-wave interaction where a gyrotron beam, polarized in X-mode, decays into two UH waves at approximately half frequency. As with all other nonlinear interactions, the onset of a TPDI occurs if the gyrotron power exceeds a threshold, determined by the coupling strength of the three waves and the interaction time with the daughter waves. The latter is determined by both linear damping and convection and diffraction of the daughter waves out of the interaction region. For many years, little attention was paid to TPDIs during ECHR, as the decay was thought insignificant due to large convection losses, resulting in power thresholds an order of magnitude above the gyrotron power [7]. The critical detail that can lower the power threshold dramatically is that UH waves can be trapped in a radial cavity inside concave density fluctuations occurring close to the second harmonic UH resonance, as illustrated in figure 1. If the gyrotron beam decays into eigenmodes of the cavity, the radial convection losses of the UH waves are eliminated, and the power threshold reduces to levels often well below 100 kW [7], i.e. an order of magnitude below the power level of modern

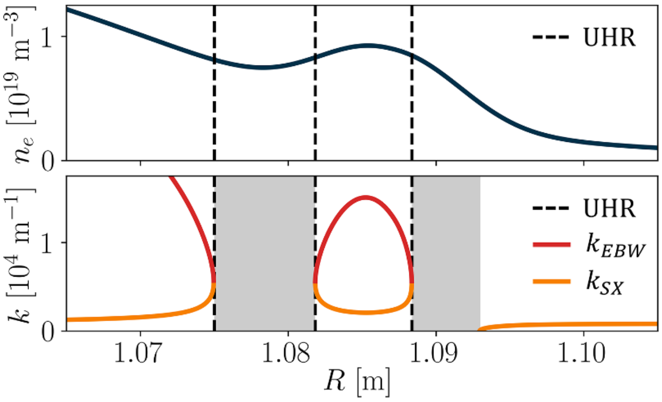

Figure 1. Example of the radial wavenumber of an UH wave, i.e. a coupled slow X (SX) and electron Bernstein wave (EBW), trapped inside a density fluctuation in the SOL between two evanescent regions (gray). The wavenumbers are calculated with the local dispersion relation that is employed in [14]. The shown wave is the 10th eigenmode of the cavity with a frequency of 41.37 GHz.

gyrotrons. Conditions for trapped daughter waves at half gyrotron frequency in X2 heating experiments are typically met in the SOL during the passing of the gyrotron beam by a blob filament or an ELM.

The TPDI becomes resonant when the phase matching conditions

$$\mathbf{k}_0 = \mathbf{k}_1 + \mathbf{k}_2, \qquad \omega_0 = \omega_1 + \omega_2, \tag{1}$$

are satisfied, where $(\mathbf{k}_0, \omega_0)$ are the wave vector and frequency of the pump wave, and $(\mathbf{k}_1, \omega_1)$, $(\mathbf{k}_2, \omega_2)$ are the wave vectors and frequencies of the two daughter waves. These conditions, together with the nonlinear coupling, determine the eigenmodes that are interacting. As is found in both fully kinetic simulations and reduced WKB models in [15], the set of daughter waves with the largest instability growth rate most often have slightly different frequencies. The same was demonstrated in [13].

While the theory of the TPDI is well established, there is still an ongoing debate on the exact mechanism for radiation at the UH wave frequencies to escape to the low field side, where it has been measured in both O-mode and X-mode polarization [10, 13]. Competing theories include nonlinear cross-polarization [10] and direct tunnelling of the UH waves with subsequent partial conversion to O-mode due to either reflections at the inner wall or linear X–O conversion at the density cutoff.

3. Radiometer

The second-harmonic ECRH system at TCV consists of three gyrotrons, all polarized in X-mode and located at the equatorial ports L1 and L4 and at the upper port L5, respectively. The two primary daughter waves from TPDIs have frequencies around half the gyrotron frequency. For the two types of X-2 gyrotrons that are installed at TCV, this amounts to expected TPDI daughter wave frequencies of ~41.35 GHz (for

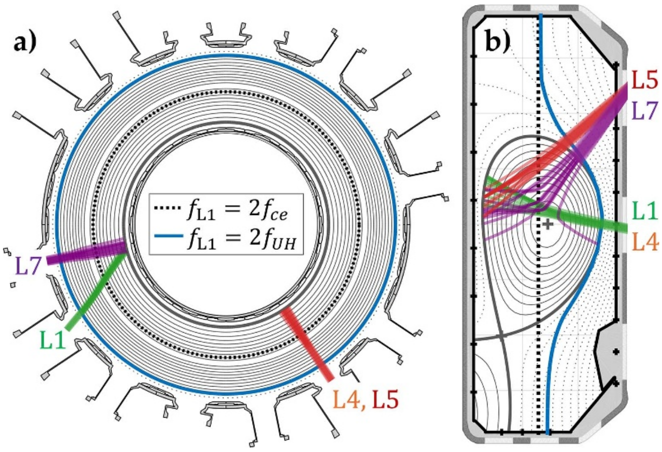

Figure 2. (a) Toroidal and (b) poloidal cross section of TCV with markings of launchers L1, L4 and L5 as well as the diagnostic launcher L7 where the heterodyne radiometer is connected. The equilibrium profile and ray tracing trajectories of the gyrotrons and LOS of the radiometer are calculated for time $t = 0.85$ s in shot #77263.

the L1 gyrotron) and ∼41.90 GHz (for the L4 and L5 gyrotrons). To measure radiation in a narrow band around these frequencies, we installed a heterodyne radiometer [16]. The radiometer is attached to an already existing transmission line from a diagnostic launcher, L7, at an upper lateral port depicted in figure 2. A diagram of the radiometer and its setup is shown in figure 3. Radiation from the plasma is collected by a steerable launcher and guided through a HE_{11} waveguide. A pair of programmable fast HE11 miter-bend polarizers make it possible to fit the mode polarization to the receiver polarization [17]. The RF signal from the waveguide is collected by a WR15 horn. From there, it is first passed through two low pass filters in order to heavily attenuate the gyrotron frequency. Afterwards, the RF signal arrives at a Q-band WR-22 balanced mixer with a frequency band of 33–50 GHz (Model QMC-MIX28-FB00 from Quantum Microwave). Here, the RF signal is mixed with a 40.245 GHz signal from a Gunn oscillator from MACOM. The output IF signal is first amplified with a series of low-noise amplifiers and is then digitized with an 8-bit 5 GS s^{-1} ADC (model M4x.2233-x4 from Spectrum Instrumentation) with an on-board memory of 4 GB. The WR-15 horn works as a high-pass filter, which limits the effective bandwidth of the radiometer to 41.1 GHz − 42.4 GHz. In order to comply with the memory limits of the digitizer, data is typically collected in many short acquisitions of $t_{ac} < 1$ ms with an overall duty cycle of 10% − 20%. A spectrogram is calculated for each acquisition, typically with an FFT window of 2^{11} samples, giving a frequency resolution of 2.44 MHz and a time resolution of 0.36 μs.

4. Calibration with ECE

4.1. Method

The signal that the radiometer is measuring contains both a background signal of amplified noise $B(\omega)$ and radiation from the plasma with radiation temperature $T_r(\omega)$. The power spectral density (PSD) of the radiation signal $S(\omega)$ can be written as

$$S(\omega) = A(\omega)\, T_r(\omega) + B(\omega), \tag{2}$$

where $A(\omega)$ is a linear mapping between the radiation temperature and the measured signal at a given frequency ω. The mapping $A(\omega)$ can be determined by measuring thermal radiation in a calibration experiment as

$$A(\omega) = \frac{S_0(\omega) - B(\omega)}{T_{r0}(\omega)}. \tag{3}$$

If the radiation temperature, T_{r0}, in the calibration experiment is known.

A calibration procedure that is often used for the radiometer in CTS systems is a two-point measurement of blackbody radiation from two microwave absorbers, one at room temperature and one cooled with liquid nitrogen [18]. This technique is relatively simple, but typically does not cover the entire transmission line and relies on a linear extrapolation between radiation at room temperature and at hundreds of eV. We therefore instead developed a calibration procedure based directly on measurements of ECE and modelling of the radiation temperature with ray tracing.

The thermal radiation along a path can be described by the equation of radiative transfer. In the long wavelength (Rayleigh–Jeans) limit, ($\hbar\omega \ll T_r$), this equation has the general steady state solution [19, 20]

$$T_r(\omega, s) = T_r(\omega, s_0)\, e^{-\tau(\omega,s,s_0)} + \frac{8\pi^3 c^2}{\omega^2} \int_{s_0}^{s} \frac{j(\omega, s')}{N_r^2(\omega, s')} e^{-\tau(\omega,s',s_0)} \mathrm{d}s', \tag{4}$$

where $N_r(\omega, s)$ is the refractive index of the radiation, and $j(\omega, s)$ is the emission coefficient, both given for a ray with frequency ω evaluated at position s. c is the speed of light in vacuum, and τ is the optical thickness,

$$\tau(\omega, s, s_0) = \int_{s_0}^{s} \alpha(\omega, s')\, \mathrm{d}s', \tag{5}$$

where $\alpha(\omega, s)$ is the local absorption coefficient, with the integral being along the radiation path from position s_0 to s. We shall assume that the plasma is in local thermodynamic equilibrium, where thermal radiation is described by Kirchhoff's radiation law, which in the Rayleigh–Jeans limit reads [20]

$$\frac{j(\omega, s)}{\alpha(\omega, s)} = \frac{\omega^2}{8\pi^3 c^2} T_e(s), \tag{6}$$

where $T_e(s)$ is the local electron temperature. Inserting equation (6) in equation (4) yields

$$T_r(\omega, s) = T_r(\omega, s_0)\, e^{-\tau(\omega,s,s_0)} + \int_{s_0}^{s} T_e(s')\, \alpha(\omega, s')\, e^{-\tau(\omega,s',s_0)} \mathrm{d}s'. \tag{7}$$

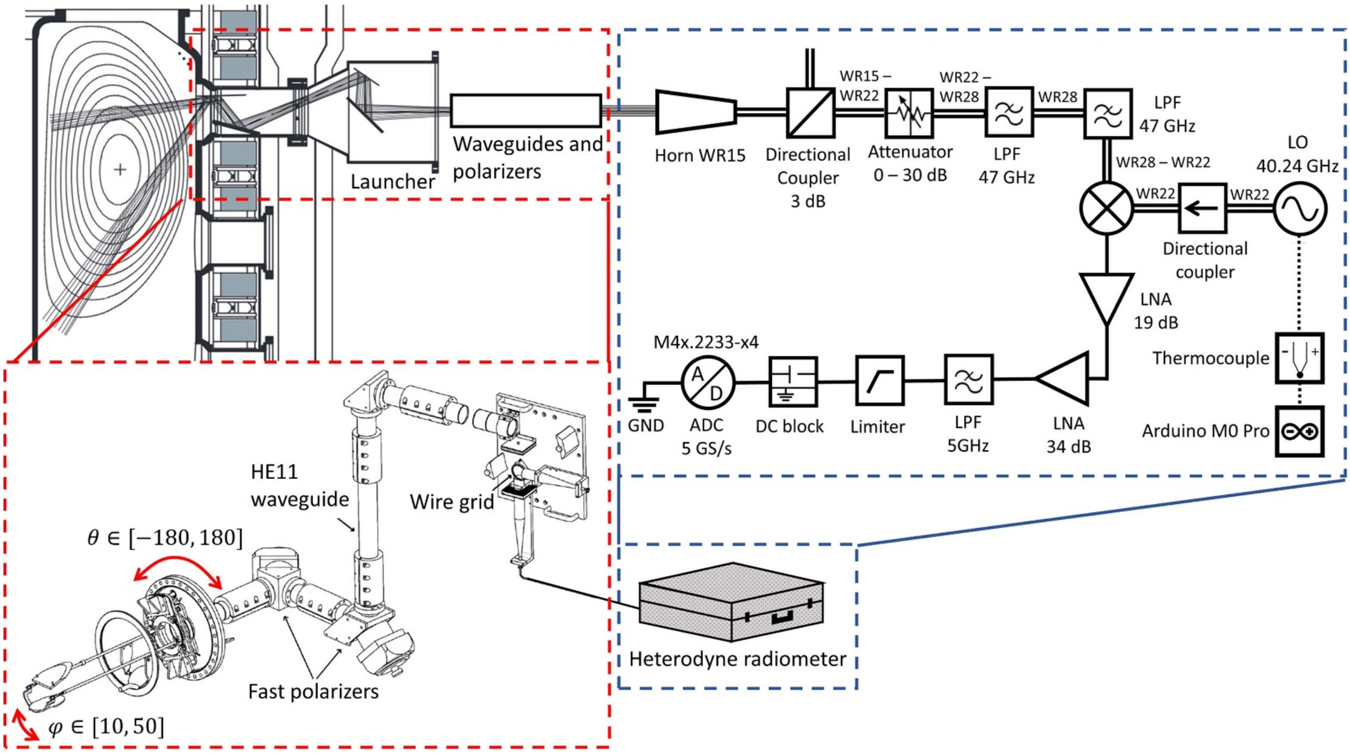

Figure 3. Diagram of the heterodyne radiometer. The upper left sketch of the L7 launcher antenna as well as the sketch of the waveguides and polarizers. Reprinted from [17], with the permission of AIP Publishing.

With the use of ray tracing, both $T_e(s)$ and $\alpha(\omega, s)$ (calculated from the local dielectric tensor) can be evaluated along a ray path in a plasma equilibrium, and the corresponding $T_r(\omega, s)$ can be evaluated with equation (7). Our calculations were carried out using the ray tracer *Warmray*, written by Henrik Bindslev. The code is not published but has been used for numerous CTS studies (e.g. [11, 21]) and its evaluation of T_r has been benchmarked against the code SPECE [22].

One complication for the evaluation of T_r in our calibration experiment is that for the LOS of the receiver, the plasma is optically thin within the radiometer bandwidth. Therefore, multiple reflections of the ray at the first wall are included in the calculation of T_r, and individual ray segments are traced between reflection points. The same approach was used for modelling ECE below the fundamental resonance in ITER [22] and DEMO [23].

The simplest way to evaluate T_r along the radiometer LOS is to trace the radiation backwards in time, i.e. by following a ray originating from the radiometer with polarization similar to the measured radiation and tracking all its reflections, ray segment by ray segment. All ray segments are reflected unless the ray segment contains less than 2% of the initial power content. In each reflection of the ray, it becomes cross-polarized, i.e. a fraction of power is reflected with a polarization in O-mode and another fraction in X-mode. The fractions of O-mode and X-mode are calculated from the boundary conditions of the first wall.

TCV has a graphite first wall with a coverage of $> 90\%$. For a plain graphite surface, the reflectance of microwaves at $\sim$40 GHz is above 0.99 [24]. Therefore, to a first approximation, the reflection angle and cross-polarization are calculated by simply assuming a perfect conductor. This method, however, overlooks the fact that the first wall has plenty of tile gaps and a large number of ports with varying sizes, acting as microwave sinks. Moreover, we shall approximate the poloidal cross section of TCV as a rectangle with walls at $R = 0.614$ m, $R = 1.147$ m, and $Z = \pm 0.76$ m. To account for these crude approximations, we chose each reflection angle as a random sample from a Gaussian distribution with a mean of the geometric optics reflection angle and a standard deviation of $\sigma_r = 10°$. We furthermore assume an effective wall reflectance of $R = 0.95$. This number should be regarded with a large uncertainty. $T_{r0}(\omega)$ is determined by an ensemble average of 20 ray tracings at each ω.

We shall denote the fraction of reflected power in the previous reflection of a ray segment n as F_n. Then, using equation (7) the radiation temperature of the total EC radiation reaching the launcher is given by

$$T_r(\omega) = \sum_n^N T_{r,n} F_n R \prod_{m \in \text{parents}} F_m R e^{-\tau(\omega, s_m, s_{m-1})} \quad (8)$$

where $T_{r,n}$ is the increment of the radiation temperature by the passing of ray segment n (following the second term in equation (7)), the parent ray segments m are all the ray segments between the considered segment and the launcher, and N is the total amount of traced ray segments.

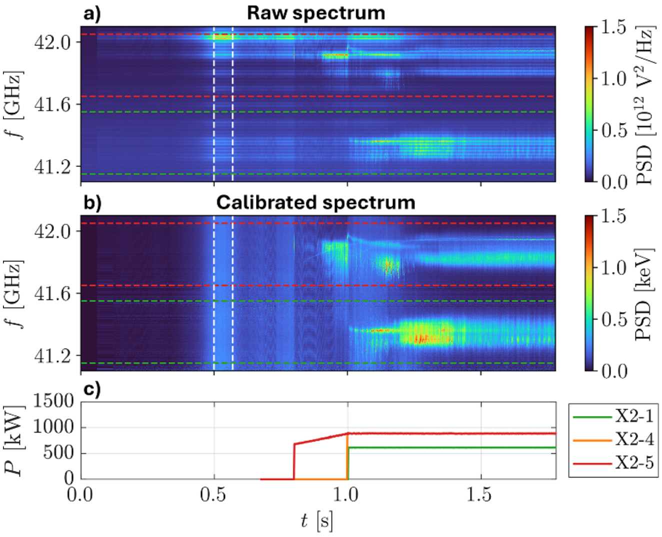

Figure 4. (a) Spectrum of the raw radiometer signal in shot #77335. (b) Same spectrum after the calibration procedure. The two white lines mark the fraction of the signal used for the calibration. The red lines mark a frequency range where daughter waves from TPDIs of L4 and L5 are produced, and the green lines mark a frequency range where daughter waves from TPDIs of L1 are produced. (c) Gyrotron power during the shot.

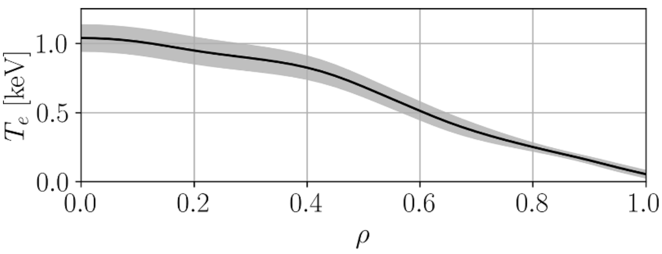

Figure 5. Temperature profile in shot #77335 at time $t = 0.50\,$s calculated from Thomson scattering.

4.2. Calibration discharge

For the calibration, we use ECE measurements in the shot #77335. The launcher was pointing into the vessel with a toroidal angle of $\theta = 0°$ and a poloidal angle of $\phi = 30°$ with the fast polarizers in O-mode. It should be noted that this approach is also possible with the polarizers in X-mode, but extra care must be taken as fundamental X-mode radiation is in cutoff. A spectrum of the raw radiometer data collected in the shot is shown in figure 4(a). The spectrum is computed by first taking a spectrogram of each individual acquisition with an FFT window of 2^{11} samples and subsequently averaging each spectrogram on the time axis to combine them into a single spectrum.

Half a second into the shot at a time before any of the gyrotrons switch on (see figure 4(c)), the radiometer measures a strong ECE signal across the entire radiometer bandwidth, which we use for calibration.

Figure 5 shows the temperature profile in the equilibrium of #77335 at time $t = 0.50\,$s, and figure 6 shows ray trajectories of O-mode radiation at the LOS of the launcher for $f = 40.5\,$GHz , yielding $T_{r0} = 283\,$eV. This is well below the

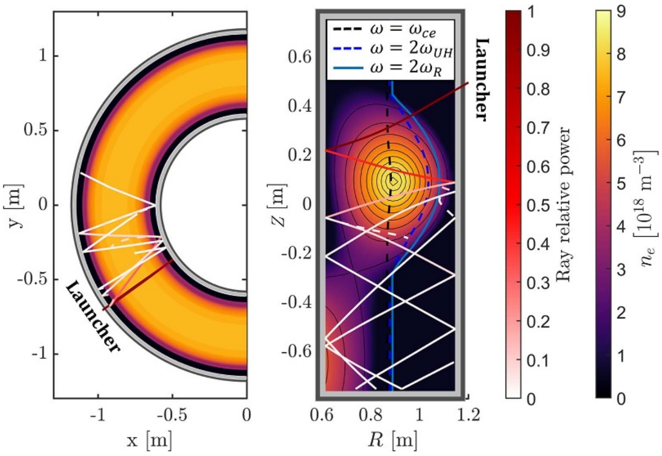

Figure 6. Ray trajectories in the toroidal plane (left) and poloidal plane (right) for a tracing of O-mode radiation with $f = 40.5\,$GHz at time $t = 0.50\,$s in shot #77335. The left colorbar maps the remaining relative power in the ray, and the right colorbar maps the plasma density. O-mode rays are solid lines, and X-mode rays are dashed lines. The simulation gives a radiation temperature of $T_r = 283\,$eV.

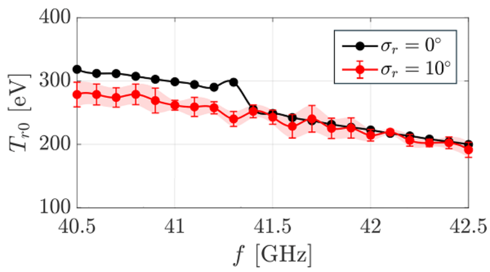

Figure 7. Calculated radiation temperature $T_{r0}(f)$ based on the ECE analysis in calibration shot #77335. $T_{r0}(f)$ is shown for both the geometric optics reflection angle ($\sigma_r = 0°$) and for reflection angles with a standard deviation of $\sigma_r = 10°$, which is used in the further analysis.

central electron temperature, owing to the fact that the plasma is optically thin at this frequency. The radiation temperature $T_{r0}(\omega)$ resulting from similar traces at different ω is shown in figures 7 and 8 shows the corresponding coefficient $A(\omega)$ following from equation (3). This coefficient, along with a background measurement, is used to calibrate the radiometer signal, yielding the spectrum shown in figure 4(b). In this figure, a clear signal from TPDI daughter waves appears around half gyrotron frequency, correlated with the time each gyrotron switches on.

5. Radiation from TPDIs in blobs

The radiometer has been used to collect radiation from TPDI daughter waves in a large series of shots with X2 heating at TCV. In these shots, TPDIs have been shown to occur in the SOL during both L-mode and H-mode operation due to trapping of the daughter waves in density fluctuations created by blobs and ELMs, respectively. Both of the two primary daughter waves were identified and shown to have a small frequency

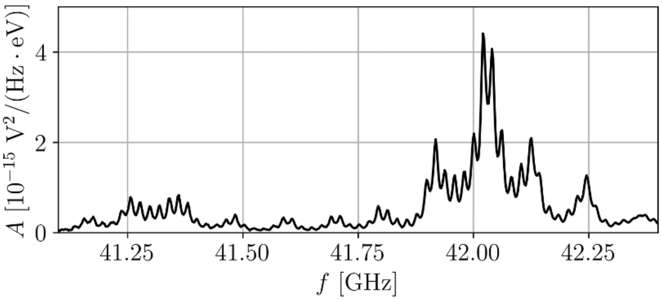

Figure 8. Coefficient $A(\omega)$ based on ECE analysis in #77335.

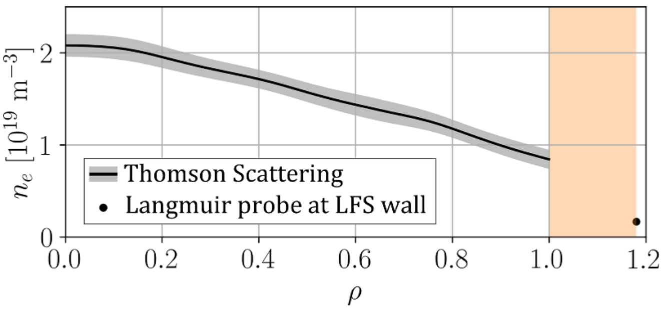

Figure 9. Density profile from Thomson Scattering as well as a density reading with a Langmuir probe located at the equatorial midplane on the low field side ($R = 1.138$ m, $z = 0.046$ m, both at $t = 0.85$ s in shot #77263. In the scrape-off layer (orange shaded region), no diagnostics for the plasma density are available in this shot.

difference depending on the density and location of the density fluctuation. For this analysis, we refer the reader to [13].

Here, we point the attention to the measurements of TPDI daughter waves in the L-mode phase of shot #77263. In the time interval $t \in [0.8, 0.9]$ s, the shot is in L-mode. A density reading from a Thomson scattering system as well as a Langmuir probe at $t = 0.85$ s is shown in figure 9. At this time, the L1 gyrotron was firing with a power of $P_0 = 613$ kW from the outer equatorial midplane. The radiometer was taking acquisitions of 0.10 ms with 0.36 ms between acquisitions. Figure 10 shows examples of radiometer acquisitions taken in this time interval, where many small events with two waves chirping around half gyrotron frequency are observed. As was demonstrated in [13], these waves are consistent with the expected frequencies of trapped UH waves generated in TPDIs as the gyrotron beam passes blob filaments in the SOL.

To further demonstrate that the TPDIs are consistently triggered by the passing of blob filaments, we consider the distribution of the signals. To do so, we take the moving average of the PSD of the radiometer signal for $f \in [41.15, 41.55]$ GHz with a window length of 10 data points and group it into either an 'event' for a moving average above 0.8 keV or 'no event' for lower PSDs. An example is shown in figure 11, where five 'events' are detected.

The two relevant quantities to consider are the waiting times between events τ_{wait} and the duration of the events τ_{event}

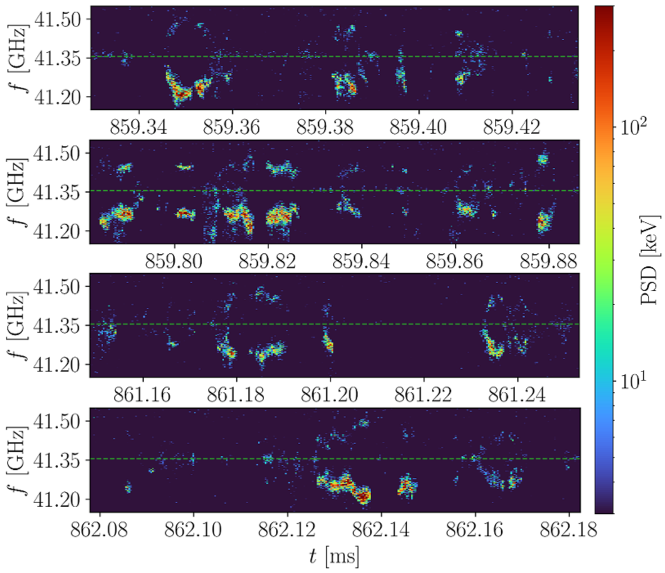

Figure 10. Spectrograms of single radiometer acquisitions in the frequency band around half the frequency of the L1 gyrotron, marked with a green line, in shot #77263.

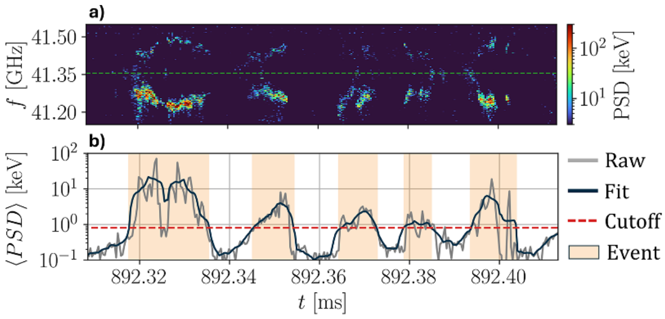

Figure 11. (a) Spectrogram of a single radiometer acquisitions in the frequency band $f \in [41.15, 41.55]$ GHz around half the frequency of the L1 gyrotron, marked with a green line, in shot #77263. (b) Average PSD of the radiometer signal in the bandwidth (grey). The dark blue line shows a moving average with a Savgol filter with a window length of 10 data points, and the red dashed line at 0.8 keV is a cutoff separating an 'event' from 'no event'.

and their distributions. Stochastic modelling as well as experimental data from TCV [25] finds the waiting time between blob events τ_{wait} to be exponentially distributed, i.e. following

$$f(t;\lambda) = \lambda e^{-\lambda t}, \tag{9}$$

where λ is a rate parameter. Additionally, Langmuir probe measurements of blobs typically have PDFs following a gamma distribution

$$f(t;\alpha,\lambda) = \frac{t^{\alpha-1}\lambda^{\alpha}e^{-\lambda t}}{\Gamma(\alpha)}, \tag{10}$$

where α is a shape parameter and λ is a rate parameter.

Figure 12 shows a histogram of both τ_{wait} and τ_{event} for $t \in [0.8, 0.9]$ s. The waiting time τ_{wait} follows an exponential distribution with rate parameter $\gamma^{-1} = 11.9\,\mu$s, and the event duration τ_{event} follows a Gamma distribution with rate parameter

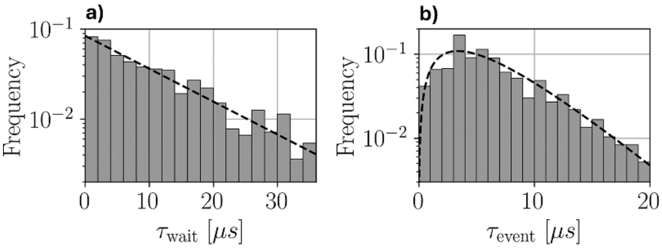

Figure 12. Histograms of (a) waiting time between signals, τ_{wait}, and (b) event duration τ_{event} for $t \in [0.8, 0.9]$ s and $f \in [41.15, 41.55]$ GHz in shot #77263. The frequencies are normalized such that the total area is 1. τ_{wait} is seen to roughly follow an exponential distribution (equation (9)) with rate parameter $\gamma^{-1} = 11.9 \pm 0.5\,\mu$s, and τ_{event} follows an Gamma distribution (equation (10)) with shape parameter $\alpha = 2$ and rate parameter $\gamma^{-1} = 3.4 \pm 0.2\,\mu$s.

$\gamma^{-1} = 3.4\,\mu$s. Thus, the measured events follow the same characteristics as blobs in the SOL, which suggests that the TPDI signal is indeed correlated with blob filaments passing the gyrotron beam.

6. Capability as a diagnostic for edge density fluctuations

As demonstrated above, the radiometer is able to detect density fluctuations due to blob filaments in the SOL. In addition to detecting when density fluctuations, due to e.g. blobs and ELMs, are crossing the gyrotron beam, the frequency difference between the two primary daughter waves also contains information on both the size and location of the density fluctuation.

In this paper, we will not present a WKB model describing TPDIs as this can be found elsewhere, e.g. [7, 15]. Here, we simply note that the nonlinear coupling coefficients between the interacting waves, ν_{12}, ν_{21}, take the form (equation (5) in [13])

$$\nu_{jj'} \propto \int_{x_l}^{x_r} \Upsilon(x)\, \mathrm{e}^{\mathrm{i}\int^x \left(k_{0,x} - k_{1,x}^{\mathrm{EBW}} - k_{2,x}^{\mathrm{EBW}}\right)\mathrm{d}x'}\, \mathrm{d}x \qquad (11)$$

where the integration bounds x_l, x_r are the ends of the region where both daughter waves exist (see figure 13), $k_{0,x}$ is the wavenumber of the pump wave, $k_{1,x}^{\mathrm{EBW}}, k_{2,x}^{\mathrm{EBW}}$ are the wave numbers of the electron Bernstein wave (EBW) branches of the two daughter waves, and $\Upsilon(x)$ depends on the background magnetic field, the plasma density, and the gyrotron power.

We shall now consider which frequencies of the two daughter waves give rise to the largest nonlinear coupling (equation (11)) for different density fluctuations. We consider a small density structure with the Gaussian shape

$$n_{\mathrm{e}}(x) = n_0 e^{-\frac{(x-x_0)^2}{\sigma^2}}, \qquad (12)$$

where n_0 is the peak density of the structure at position x_0, and σ is the width of the structure. We have here neglected the background density, as this plays no role for the two-plasmon

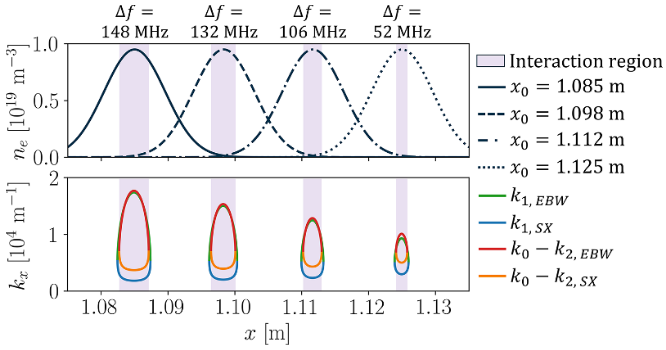

Figure 13. wavenumbers of the two primary TPDI daughter waves trapped inside a Gaussian density structure (equation (12)) with $n_0 = 0.95 \cdot 10^{19}\,\mathrm{m}^{-3}$ and $\sigma = 0.01$ m for structures at four different positions x_0. The frequency difference between the daughter waves is optimized to give the largest nonlinear coupling (equation (11)). The calculations use $T_{\mathrm{e}} = 100$ eV and $\mathbf{B} = B_0 R_0 / x\, \hat{\mathbf{z}}$ with $B_0 = 1.433$ T and $R_0 = 0.88$ m.

decay process. For simplicity, we restrain the analysis to 1D and neglect mode quantization.

In figure 13, a density structure is plotted at four different radial positions with the background B-field mimicking the SOL in the equatorial midplane of TCV and the electron temperature T_{e} set to 100 eV. The widths of the density structures are set to $\sigma = 1$ cm, in accordance with the typical radial size of blob structures in TCV [26]. For each position of the density structure, the wavenumbers of the two primary trapped TPDI daughter waves are plotted using the local dispersion relation that is employed in [14]. The frequency difference between the daughter waves is optimized to give the largest possible nonlinear coupling (equation (11)). As is seen in the figure, the coupling is generally largest when there is a good k-match between the EBW branches of the two daughter waves. As a result, the frequency difference gets smaller and smaller when the density structure is located at a larger x, because the lower B-field gives rise to smaller wavenumbers.

Figure 14 shows a parameter scan of the expected frequency difference as a function of both location, x_0, and peak density, n_0, of the Gaussian density structure. The frequency shifts are seen to be highly systematic, with larger Δf generally happening for larger n_0 and lower x_0. Accordingly, it is possible to extract information on the fluctuation level of density perturbations in the plasma edge that give rise to TPDIs observed by the radiometer.

To do so, we consider the distribution of the frequency differences between the two primary daughter waves of each event for $t \in [0.8, 0.9]$ s and $f \in [41.15, 41.55]$ GHz in shot #77263. As can be seen in figure 10, the frequency difference chirps within each event due to the movement of the blob filament through the gyrotron beam. The best indicator for the size of the density structure is the maximum frequency difference between the two daughter waves. As the signal has a relatively low signal-to-noise ratio, this is evaluated in the following systematic way: For each event, the PSD of the signal is averaged in time. Then, the lowest frequency of the low-frequency daughter wave, f_{low}, is evaluated as the frequency where a moving average of the time-averaged PSD

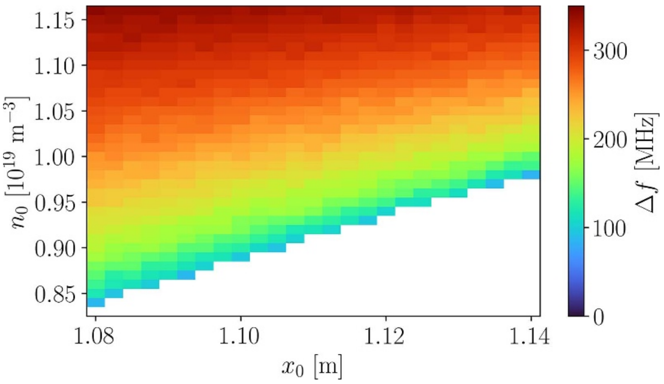

Figure 14. Frequency difference between the two primary TPDI daughter waves trapped inside a Gaussian density structure according to equation (12) with $\sigma = 0.01$ m for different positions x_0 and peak densities n_0. The calculations use $T_e = 100$ eV and $\mathbf{B} = B_0 R_0 / R\, \hat{\mathbf{z}}$ with $B_0 = 1.433$ T and $R_0 = 0.88$ m.

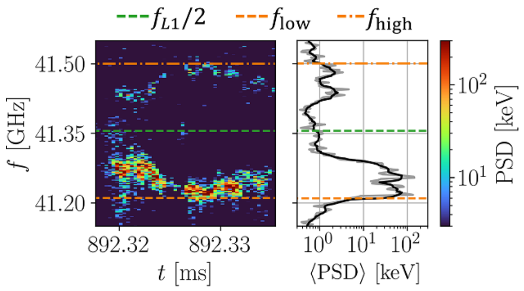

Figure 15. Left: spectrogram of a single event. Right: raw signal (gray) and moving average with a window length of 6 (black) of the time averaged PSD during the event. The green line marks half the frequency of the L1 gyrotron, the orange dashed line marks the evaluated lowest frequency of the low frequency daughter wave f_{low}, and the orange dashdotted line marks the evaluated highest frequency of the high frequency daughter wave f_{high}.

crosses half of its maximum value. Finally, the highest frequency of the high-frequency daughter wave, f_{high}, is evaluated by simply mirroring f_{low} around half the frequency of the L1 gyrotron, and the maximum frequency difference is calculated as $\Delta f_{\mathrm{max}} = f_{\mathrm{high}} - f_{\mathrm{low}}$. This procedure is illustrated in figure 15.

The resulting distribution of maximum frequency differences Δf_{max} is shown in figure 16. The distribution is relatively broad, with a peak around 220 MHz and a cutoff at 380 MHz. The last closed flux surface is located around $R = 1.08$ m in the outer equatorial plane for $t \in [0.8, 0.9]$ s. As the peak density of blob filaments generally decreases with distance into the SOL, most TPDIs are expected to occur around $R \in [1.07, 1.11]$ m in this time interval. Based directly on the plot in figure 14, the typical Δf_{max} of 220 MHz suggests a fluctuation level with typical peak densities around $n_{\mathrm{fluctuation,typical}} \sim 1 \cdot 10^{19}\,\mathrm{m}^{-3}$ and the distribution in figure 16 suggests that most peak fluctuation densities range within $n_{\mathrm{fluctuation}} \in [0.9, 1.1] \cdot 10^{19}\,\mathrm{m}^{-3}$. This density range is consistent with the density in the edge of the confined plasma in figure 9 as well as interchange turbulence simulations of blobs in this particular shot [13]. As no density measurements were available in the SOL region in the

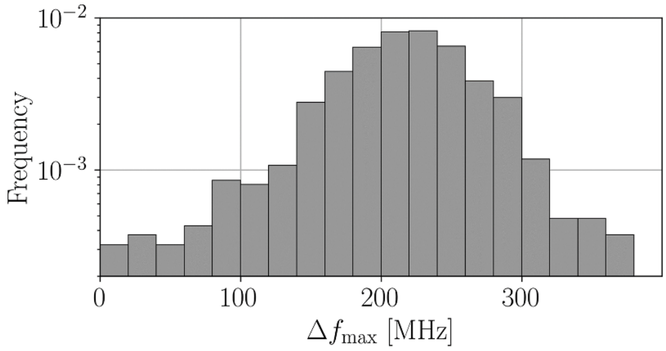

Figure 16. Distribution of the frequency differences between the two primary daughter waves in each event for $t \in [0.8, 0.9]$ s and $f \in [41.15, 41.55]$ GHz in shot #77263. The frequency differences are calculated by the method illustrated in figure 15.

shot, a direct comparison of the between density estimation from two-plasmon decays and probe readings of individual blob filaments remains a subject for further studies.

It should be emphasized that this is a very simplified model based on reduced dimensionality and an extremely crude approximation of the blob shape. Furthermore, the poloidal *B*-field as well as electron temperature variation were omitted for simplicity. The overall method of using the radiometer to estimate the density fluctuation level in the plasma edge is, however, promising.

In addition to diagnosing the overall fluctuation level, the radiometer signal also contains information on the temporal evolution of each density fluctuation that passes the gyrotron beam and gives rise to a TPDI. The problem of reconstructing the detailed density profile and exact location of such a density fluctuation is, however, ill-posed. Filaments from blobs and ELMs move not only radially but also poloidally, and density profiles come in a large variety. Additionally, the effects of quantization and higher dimensionality, which have here been neglected, both add further complications. With more advanced modelling and the possible use of artificial intelligence, substantial information on the evolution of density structures in the plasma edge could, in principle, be obtained.

A different approach is to start with a simulation of turbulent structures in the SOL based on parameters from plasma diagnostics. By applying forward modelling, the frequency of the daughter waves from TPDIs can be predicted and compared to the radiometer measurements. This is done for a single blob structure in [13] using the interchange turbulence code HESEL [27]. One could imagine a similar analysis for a long simulation, where distributions of e.g. waiting times, event duration, and frequency differences could be compared.

As a final remark, we stress that the method presented here is not applicable for diagnosing blob filaments and ELM filaments in the SOL region. By moving the location of the second harmonic UH layer of a gyrotron beam further into the plasma, concave density perturbations in the core region due to e.g. magnetic islands could be analysed as well [5, 6]. This can be achieved by operating with a higher gyrotron frequency or, simply, by performing experiments at a reduced magnetic field.

7. Conclusion

A heterodyne radiometer diagnostic was installed at the TCV tokamak to diagnose daughter waves from TPDIs with frequencies around half the gyrotron frequency. The radiometer was calibrated with ECE measurements combined with a ray tracing analysis to calculate the radiation temperature based on the equation of radiative transfer. The radiometer has successfully identified both primary daughter waves resulting from TPDIs due to trapping of UH waves in blob filaments.

The two primary daughter waves have a small frequency difference, depending on the density and location of the blob. Based on this feature, we demonstrate that the radiometer can be used as a diagnostic for density fluctuations in the plasma edge due to blobs and ELMs that occur during operation with X2 ECRH.

A similar radiometer could easily be implemented on other ECRH devices. With a different gyrotron frequency or lowered magnetic field, this method could also be used to diagnose concave density fluctuations in the confined plasma, e.g. due to rotating islands.

Data availability statement

The data cannot be made publicly available upon publication due to legal restrictions preventing unrestricted public distribution. The data that support the findings of this study are available upon reasonable request from the authors.

Acknowledgments

We thank Kenneth Lee for his assistance with the Langmuir probe analysis. This work has been supported by research Grant 15483 from VILLUM FONDEN and Grant CF23-0181 from the Carlsberg Foundation. This work has been carried out within the framework of the EUROfusion Consortium, partially funded by the European Union via the Euratom Research and Training Programme (Grant Agreement No 101052200 - EUROfusion). The Swiss contribution to this work has been funded by the Swiss State Secretariat for Education, Research and Innovation (SERI). Views and opinions expressed are however those of the authors only and do not necessarily reflect those of the European Union, the European Commission or SERI. Neither the European Union nor the European Commission nor SERI can be held responsible for them. This work was supported in part by the Swiss National Science Foundation.

ORCID iDs

A Clod https://orcid.org/0000-0002-2476-9856
R Ragona https://orcid.org/0000-0002-3225-5732
M G Senstius https://orcid.org/0000-0001-9596-7457
T Jensen https://orcid.org/0000-0001-9801-1530
U Kumar https://orcid.org/0000-0002-3258-8078
S Coda https://orcid.org/0000-0002-8010-4971
S K Nielsen https://orcid.org/0000-0003-4175-3829

References

[1] Rosenbluth M N 1972 *Phys. Rev. Lett.* **29** 565
[2] Lee Y C and Kaw P K 1974 *Phys. Rev. Lett.* **32** 135
[3] Porkolab M and Cohen B I 1988 *Nucl. Fusion* **28** 239
[4] Yu Popov A and Gusakov E Z 2015 *Plasma Phys. Control. Fusion* **57** 025022
[5] Westerhof E *et al* 2009 *Phys. Rev. Lett.* **103** 125001
[6] Nielsen S K *et al* 2013 *Plasma Phys. Control. Fusion* **55** 115003
[7] Gusakov E Z and Popov A Y 2020 *Phys.-Usp.* **63** 365
[8] Tancetti A *et al* 2022 *Nucl. Fusion* **62** 074003
[9] Tancetti A *et al* 2023 *Plasma Phys. Control. Fusion* **65** 15001
[10] Hansen S K *et al* 2020 *Nucl. Fusion* **60** 106008
[11] Nielsen S K *et al* 2016 *Phys. Scr.* **92** 24001
[12] Reimerdes H *et al* 2022 *Nucl. Fusion* **62** 42018
[13] Clod A *et al* 2024 Phys. Rev. Lett. **132** 135101
[14] Gusakov E Z and Popov A Y 2016 *Phys. Plasmas* **23** 082503
[15] Senstius M G *et al* 2022 *Plasma Phys. Control. Fusion* **64** 115001
[16] Hartfuss H J *et al* 1997 *Plasma Phys. Control. Fusion* **39** 1693
[17] Molina Cabrera P *et al* 2018 *Rev. Sci. Instrum.* **89** 83503
[18] Stejner M *et al* 2014 *Rev. Sci. Instrum.* **85** 93504
[19] Befki G 1966 *Radiation Processes in Plasmas* (Wiley)
[20] Hartfuß H-J and Geist T 2013 *Fusion Plasma Diagnostics With mm-Waves* (Wiley-VCH)
[21] Bindslev H *et al* 1999 *Phys. Rev. Lett.* **83** 3206
[22] Rasmussen J *et al* 2019 *Plasma Phys. Control. Fusion* **61** 95002
[23] Rasmussen J and Korsholm S B 2024 *Nucl. Fusion* **64** 046003
[24] Papoular R J and Papoular R 2014 *Mon. Not. R. Astron. Soc.* **443** 2974
[25] Theodorsen A *et al* 2016 *Plasma Phys. Control. Fusion* **58** 44006
[26] Garcia O E *et al* 2007 *Nucl. Fusion* **47** 667
[27] Nielsen A H *et al* 2017 *Plasma Phys. Control. Fusion* **59** 025012